

# Physical Density Estimations of Single- and Dual-energy CT Using Material-based Forward Projection Algorithm

**Kai-wen Li**

Beihang University

**Daiyu Fujiwara**

Tokushima University

**Akihiro Haga** (✉ [haga@tokushima-u.ac.jp](mailto:haga@tokushima-u.ac.jp))

Graduate School of Biomedical Sciences, Tokushima University, Tokushima 770-8503, Japan

<https://orcid.org/0000-0001-9220-2862>

**Huisheng Liu**

Beihang University

**Li-Sheng Geng**

Beihang University

---

## Research

**Keywords:** CT calibration, Dual-energy CT, Biological tissue, ICRP110 human phantom, HU-to-density curve

**Posted Date:** September 8th, 2020

**DOI:** <https://doi.org/10.21203/rs.3.rs-67602/v1>

**License:**  This work is licensed under a Creative Commons Attribution 4.0 International License.

[Read Full License](#)

---

1 **Title:** Physical density estimations of single- and dual-energy CT using material-based forward  
2 projection algorithm

3 **Running Title:** Physical density estimations using material-based forward projection

4

5 **Author:**

6 Kai-Wen Li<sup>1,2</sup>, Daiyu Fujiwara<sup>3</sup>, Akihiro Haga<sup>3a</sup>, Huisheng Liu<sup>1</sup> and Li-Sheng Geng<sup>2,1,4,5</sup>

7 1. *Beijing Advanced Innovation Center for Big Data-Based Precision Medicine, School of Medicine*  
8 *and Engineering, Beihang University, Key Laboratory of Big Data-Based Precision Medicine*  
9 *(Beihang University), Ministry of Industry and Information Technology, Beijing 100191, China*

10 2. *School of Physics, Beihang University, Beijing 102206, China*

11 3. *Graduate School of Biomedical Sciences, Tokushima University, Tokushima 770-8503, Japan*

12 4. *Beijing Key Laboratory of Advanced Nuclear Materials and Physics, Beihang University, Beijing*  
13 *102206, China*

14 5. *School of Physics and Microelectronics, Zhengzhou University, Zhengzhou, Henan 450001, China*

15

16 **Corresponding Author:**

17 Akihiro Haga, Ph.D.

18 Electronic mail: [haga@tokushima-u.ac.jp](mailto:haga@tokushima-u.ac.jp)

19 Telephone number: +81 88 633 9024

20 Mailing address: 3-18-15 Kuramoto-cho, Tokushima, 770-8503, Japan

21

## 22 **Abstract**

23 **Purpose:** This study aims to evaluate the accuracy of physical density prediction in single-energy CT  
24 (SECT) and dual-energy CT (DECT) by adapting a fully simulation-based method using a material-  
25 based forward projection algorithm (MBFPA).

26 **Methods:** We used biological tissues referenced in ICRU Report 44 and tissue substitutes to prepare  
27 three different types of phantoms for calibrating the HU-to-density curves. Sinograms were first  
28 virtually generated by the MBFPA with four representative energy spectra (i.e. 80 kV, 100 kV, 120 kV,  
29 and 6 MV) and then reconstructed to form realistic CT images by adding statistical noise. The HU-to-  
30 density curves in each spectrum and their pairwise combinations were derived from the CT images. The  
31 accuracy of these curves was validated using the ICRP110 human phantoms.

32 **Results:** The relative mean square errors (RMSEs) of the physical density by the HU-to-density curves  
33 calibrated with kV SECT nearly presented no phantom size dependence. The kV-kV DECT calibrated  
34 curves were also comparable with those from the kV SECT. The phantom size effect became notable  
35 when the MV X-ray beams were employed for both SECT and DECT due to beam hardening effects.  
36 The RMSEs were decreased using the biological tissue phantom.

37 **Conclusions:** Simulation-based density prediction can be useful in the theoretical analysis of SECT  
38 and DECT calibrations. The results of this study indicated that the accuracy of SECT calibration is  
39 comparable with that of DECT using biological tissues. The size and shape of the calibration phantom  
40 could affect the accuracy, especially for MV CT calibrations.

41 **Keywords:** CT calibration, Dual-energy CT, Biological tissue, ICRP110 human phantom, HU-to-  
42 density curve

43

## 44 **Introduction**

45 To establish the relationship between the computed tomography (CT) number (in Hounsfield units,  
46 HU) of a given voxel and the physical (or electron) density relative to water is one of the crucial  
47 processes that control the variance of patient dose calculations in radiotherapy treatment planning<sup>1-3</sup>.

48 The HU-to-density conversion is typically determined by calibration curves, which are experimentally

49 obtained from tissue-substitutes with known densities in a calibration phantom. Several studies have  
50 investigated the sensitivity of dose calculation for photon and particle beams relative to the accuracy of  
51 this conversion<sup>4,7</sup>. A major concern of this approach is that the elemental composition of these substitutes  
52 may differ from that of biological tissues, and consequently, the adopted calibration curves may not be  
53 sufficiently accurate. One way to overcome this problem is the state-of-the-art stoichiometric calibration  
54 method introduced by Schneider et al.<sup>8</sup>, in which the specific parameters of a CT scanner are determined  
55 by the measurement of a few tissue-substitutes with known materials. Recently, this method has been  
56 re-examined in the context of single-energy CT (SECT) calibration for proton therapy treatment  
57 planning, and its accuracy was found to depend on the tissue-substitutes used for calibration<sup>9</sup>. This  
58 dependency implies that the improvement of dual energy CT (DECT) over SECT should also be re-  
59 assessed, which may depend on the use of tissue substitutes as determined in a number of experiments  
60 for predicting relative stopping powers in proton therapy<sup>10</sup>.

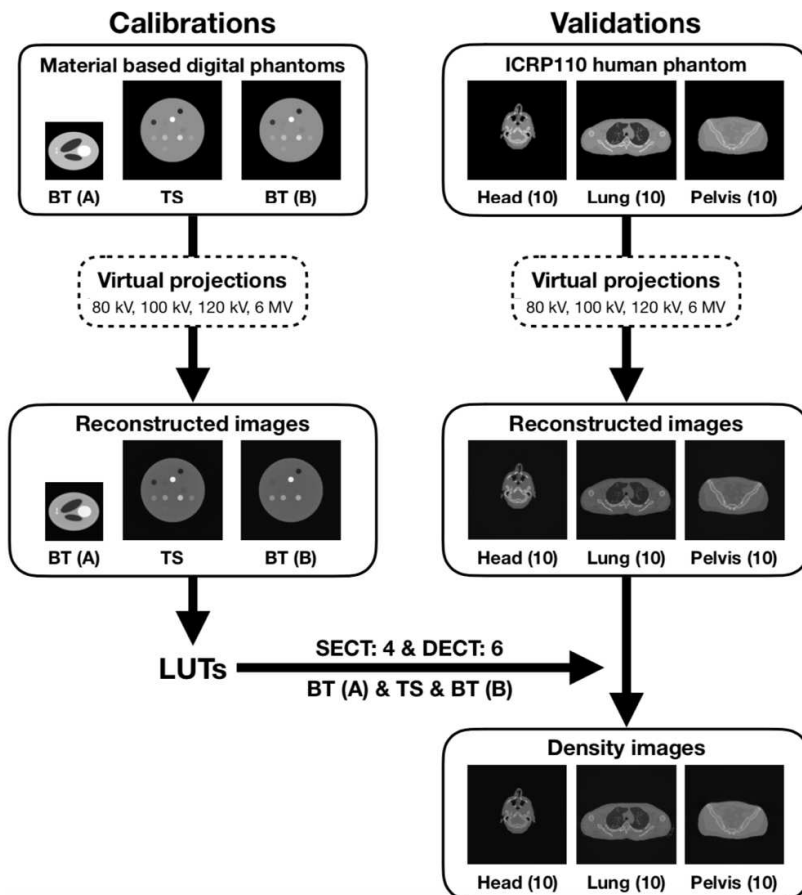
61 In this study, the accuracy of physical density prediction using SECT and DECT was evaluated, which  
62 is the first step in treatment planning. To reduce the uncertainty of the calibration, the HU-to-density  
63 conversion using biological tissues from ICRU Publication 44 was proposed<sup>11-15</sup>. The approach in this  
64 study differs from the stoichiometric calibration<sup>8</sup> by assuming that the X-ray spectra are known for the  
65 evaluation of the attenuation coefficients. In this case, CT values were reconstructed from the sinograms  
66 generated by the material-based forward projection algorithm (MBFPA), which has been utilised in  
67 model-based material decomposition<sup>16,17</sup>, when the material composition of the object was determined.  
68 These CT values were then used to perform the calibration to obtain the HU-to-density look-up-table  
69 (LUT). Using this LUT, arbitrary CT images can be converted to density images. Namely, this approach  
70 is a full simulation of the clinical process because it is based on the modelling of the entire CT system,  
71 including the incident X-ray energy spectrum.

72 The aim of this study was threefold. First, the feasibility of the proposed approach using MBFPA for  
73 physical density prediction was presented, which is significantly relevant to estimate proton stopping  
74 powers for treatment planning. To achieve this, the HU-to-density curves were simulated using three  
75 types of phantoms, where phantom (size/shape and composition) dependence in the calibration was also  
76 analysed. Second, the advantage of DECT over SECT for calibrations based on the proposed approach

77 was quantitatively evaluated. Furthermore, the issue of whether a large energy gap in DECT, such as in  
78 the kilovoltage-megavoltage (kV-MV) range, could improve the accuracy of estimating the physical  
79 density was reassessed.

## 80 **Materials and Methods**

81 The schematic workflow is shown in Fig. 1. The method starts with the preparation of three types of  
82 two-dimensional material-based digital calibration phantoms. Next, virtual projections (or sinograms)  
83 were produced using MBFPA, and CT images were sequentially reconstructed with the sinograms.  
84 Using the reconstructed images, the HU-to-density LUTs were calculated for each phantom. Finally,  
85 these LUTs were validated by predicting the physical density distributions of the ICRP110 human  
86 phantom. Four different X-ray energy sources (i.e. 80 kV, 100 kV, 120 kV, 6 MV) were employed. Thus,  
87 four SECTs and their six pairwise combinations for DECTs were considered.

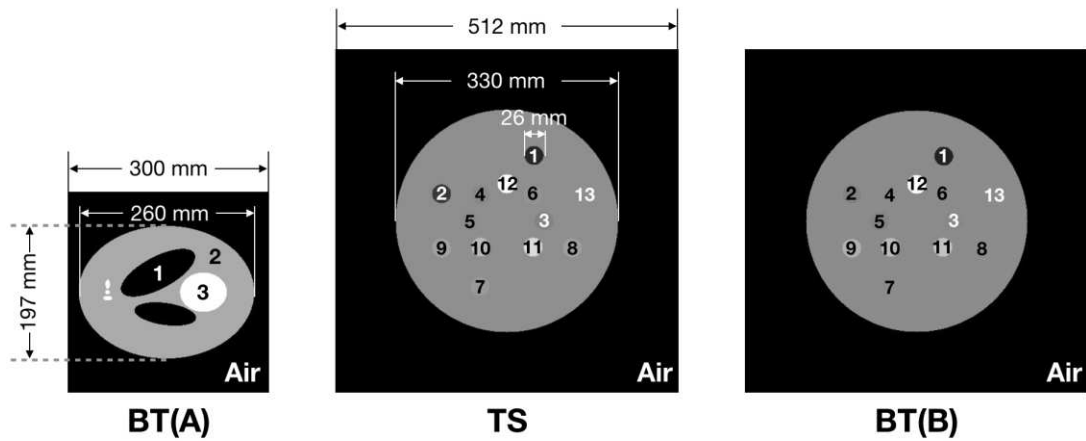


88 Fig. 1. Workflow of the current study for total density evaluation. BT(A), TS, and BT(B) phantoms were used for  
89 the calibration, and the ICRU human phantoms were used for the validation (for more details, see the main text).

## 90 **Digital phantoms**

91 Three types of phantoms were employed for the calibrations in this study, including the biological  
92 tissue (BT) phantoms in two different sizes and shapes, as well as the Gammex phantom (Gammex Inc.,  
93 Middleton, WI). The former two are referred to as the BT(A) and BT(B) phantoms, respectively. The  
94 latter is known to have better tissue substitutes (TS) than the other tissue-mimicking phantoms<sup>9</sup>, and is  
95 hereon referred to as the TS phantom. The shape of BT(A) is similar to the Shepp-Logan phantom,  
96 whereas those of TS and BT(B) mimicked that of the Gammex phantom. The composed materials of  
97 BT(A) were taken from the ICRU publication 44<sup>13-15</sup>. Details of the elemental compositions and mass  
98 fractions are listed in Table I of Ref. 11 or Table I of Ref. 12. Following Hünemohr et al.'s study<sup>12</sup>, the  
99 mass fractions of six major elements (H, C, N, O, P, Ca) were normalised to provide a sum of 100%.  
100 Three of the materials were randomly selected to construct one BT(A) phantom; a total of 54 phantoms  
101 were generated. Meanwhile, the TS phantom was composed of one base material (solid water) and 12  
102 insertions (LN-300, LN-450, AP6, BR12, water, SR2, LV1, IB3, B200, CB2-30%CaCO<sub>3</sub>, CB2-  
103 50%CaCO<sub>3</sub>, and SB3), which were generated with weight fractions and mass densities of 8 elements (H,  
104 C, N, O, Mg, Si, P, and Ca) provided in Ref.<sup>9</sup>. The BT(B) phantoms have the same shape as the TS  
105 phantom but consist of 12 standard human biological tissues<sup>13-15</sup> and water instead of tissue-substitutes.  
106 By using different biological tissues, 6 phantoms were created. The width (major axis) and height (minor  
107 axis) of each BT(A) phantom were 260 mm and 197 mm, respectively, with a pixel scale of 1 mm, while  
108 the TS and BT(B) phantoms had a radius of 115 mm. Each of the insertions in the latter two had a radius  
109 of 13 mm. All the phantoms were placed in the air to obtain “complete” phantoms (images), for which  
110 the sizes were  $300 \times 300 \text{ mm}^2$  for the BT(A) and  $512 \times 512 \text{ mm}^2$  for the TS and BT(B). These three  
111 types of phantoms were considered for the following reasons: 1) to analyse the size and shape  
112 dependence by comparing the calibration results from the BT(A) and BT(B) phantoms, and 2) to analyse  
113 the material dependence by comparing the TS and BT(B) phantoms. Finally, 30 images were prepared  
114 from the ICRP110 human phantoms for validation, which consisted of five head, lung, and pelvis  
115 phantom slices for both, females and males, which were all  $512 \times 512 \text{ mm}^2$  in size with a 1-mm scale;  
116 six elements (H, C, N, O, P, and Ca) were considered. The specifics of all the phantoms used in this  
117 study are summarised in Table 1. The phantoms in the calibration are shown in Fig. 2, and the selected

118 ICRP110 human phantoms are shown in Figs. 3 and 4.

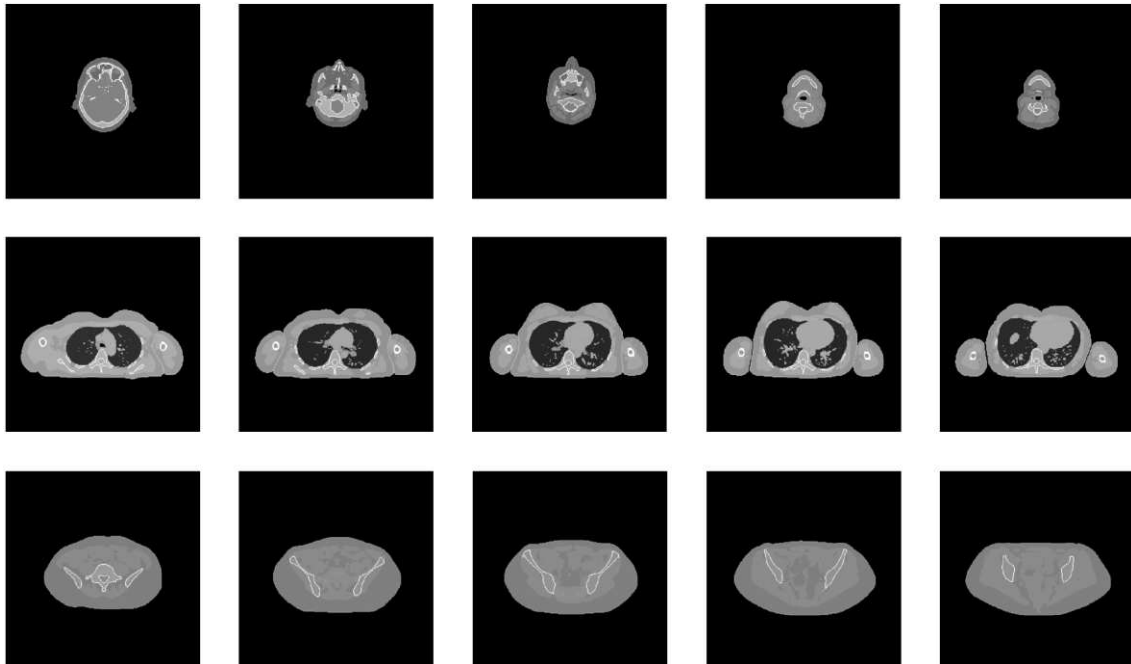


- **BT(A)** 1-3: biological tissues
- **TS** 1: LN-300, 2: LN-450, 3: AP6, 4: BR12, 5: Water, 6: SR2, 7: LV1, 8: IB3, 9: B200, 10: CB2-30%CaCO<sub>3</sub>, 11: CB2-50%CaCO<sub>3</sub>, 12: SB3, 13: Solid water
- **BT(B)** 5: Water, **Others**: biological tissues

119

120

Fig. 2. Shape, size, and composition of the BT(A), TS, and BT(B) phantoms in the calibration.

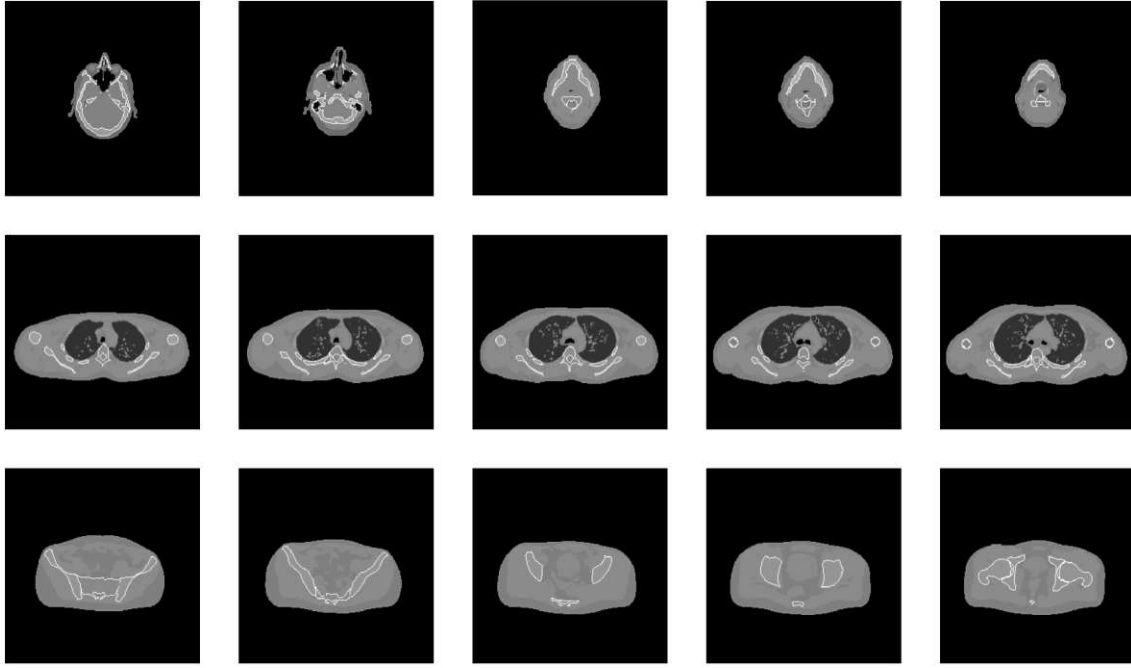


121

122

123

Fig. 3. Ground truth of the selected ICRP110 human phantoms for female. The images in the first, second, and third row indicate head, lung, and pelvis, respectively.



124

125

126

Fig. 4. Ground truth of the selected ICRP110 human phantoms for male. The images in the first, second, and third row indicate head, lung, and pelvis, respectively.

127

128

Table 1. Specifics of all the phantoms used in this study.

Name	Calibration			Validation
	BT (A)	TS	BT (B)	ICRP110 human
Materials	Biological tissues	Tissue substitutes	Biological tissues	-
Shape	Shepp-Logan	Gammex	Gammex	Head/Lung/Pelvis
Width (mm)	260	330	330	-
Height (mm)	197	330	330	-
Image (mm <sup>2</sup> )	300 <sup>2</sup>	512 <sup>2</sup>	512 <sup>2</sup>	512 <sup>2</sup>
Slice(s) <sup>†</sup>	54	1	6	30

129

<sup>†</sup>: number of phantoms (slices) used in calibration and validation.

130

131

### Virtual projection and reconstruction

132

In this study, four different X-ray energies (80 kV, 100 kV, 120 kV, and 6 MV) were used for SECTs,

133

and their six pairwise combinations for DECTs. This makes it simple to compare the results from SECT,

134

kV-kV DECT, and kV-MV DECT. For diagnostic CT, an X-ray within the MV range is not applicable,

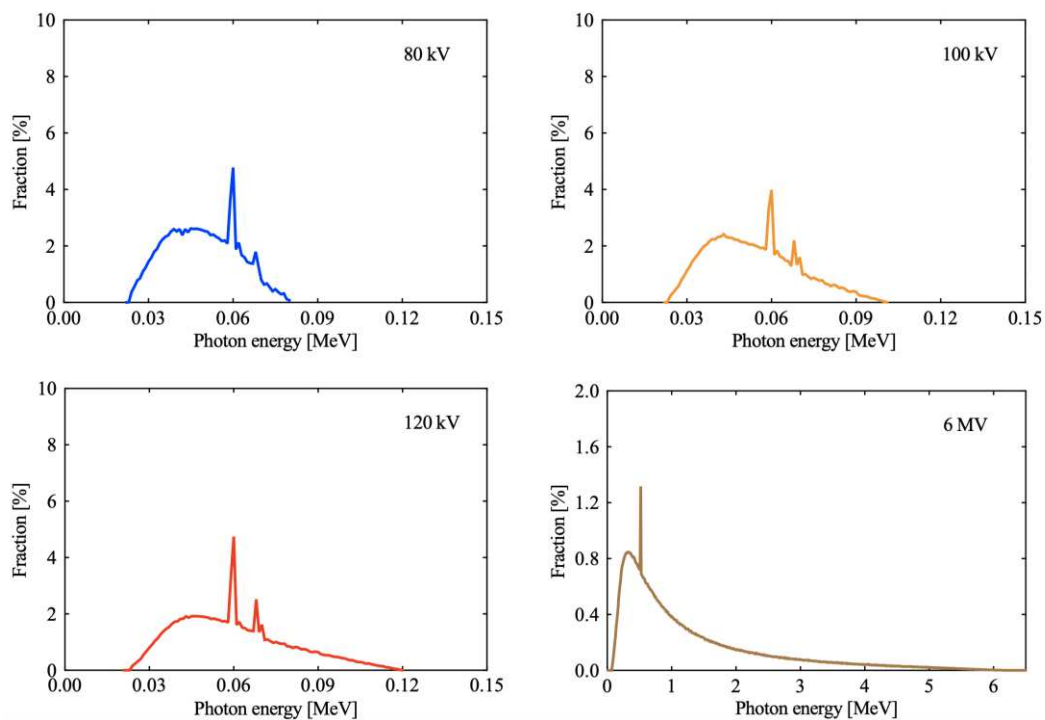
135

whereas for image-guided radiation systems, equipment to produce clinical or non-clinical projection

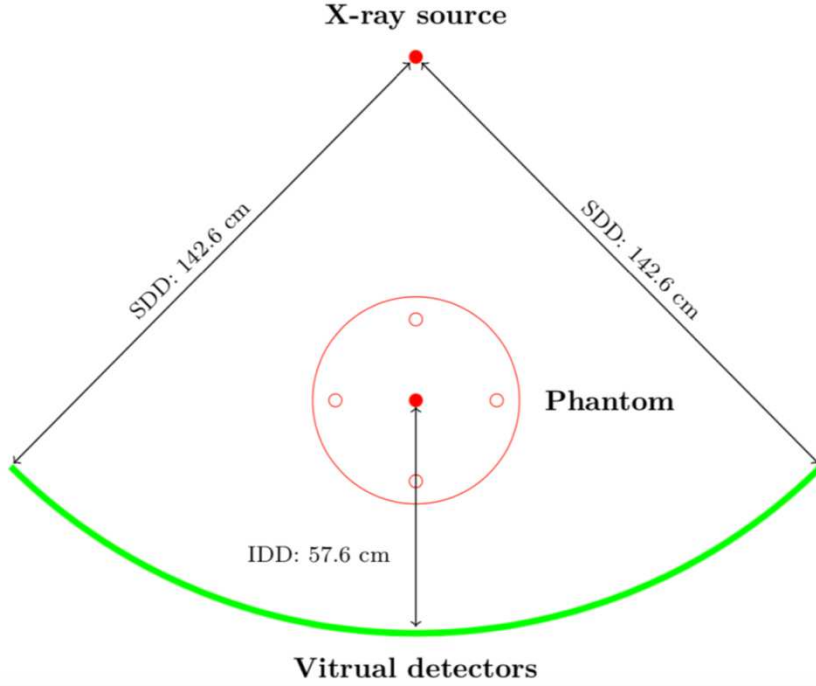
136

images with MV X-rays exists<sup>18-20</sup>. In this study, a 6 MV X-ray, which is a typical X-ray energy used in

137 radiation treatment, was selected. The spectra of the X-ray sources were obtained by Monte-Carlo (MC)  
 138 simulations using the GEANT4 toolkit (version 10.4) for a linear accelerator with kV imaging capability  
 139 (Synergy, Elekta, UK). For kV X-rays, low-energy photons generated from an anode were decimated  
 140 by filters composed of aluminium and copper, and the beam shape was formed by lead-cone and cassette  
 141 collimators. For the MV X-rays, the photons generated from the target were decimated by a flattening  
 142 filter, and the beam shape was formed by primary, jaw, and multi-leaf collimators. In both cases, the  
 143 energy spectrum was formed by the photons collected on the plane located 70 cm from the sources<sup>21</sup>.  
 144 Fig. 5 presents the X-ray spectra produced for the kV and MV beams. Using the spectra and the digital  
 145 calibration phantoms indicated above, virtual projections using MBFPA were then simulated; further  
 146 details can be found in the Appendix. The geometry of the simulated CTs with relevant factors is shown  
 147 in Fig. 6. The source and detectors were rotated 360 degrees in 0.45-degree increments (in total 800  
 148 projections). There were 609 detectors, which were aligned in equal intervals (0.15 cm). Furthermore,  
 149 random noise is inevitable in CT imaging, which is also a main source of artefacts. A Gaussian  
 150 distributed random noise was added to the sinograms (detectors) for the simulations in this study, for  
 151 which the strength was determined to produce a signal-to-noise ratio of  $\sim 20$  in the reconstructed images  
 152 of a homogeneous water phantom, which is consistent with that in clinical practice.



153 Fig. 5. Simulated X-ray spectra of 80 kV, 100 kV, 120 kV, and 6 MV. The mean energies were 48.70 keV,  
 154 53.24 keV, 59.28 keV, and 1.30 MeV, respectively.



155 Fig. 6. Schematic of geometry applied in sinogram production. IDD and SDD indicate the isocenter-to-  
 156 detector distance and the source-to-detector distance, respectively. A total of 609 detectors were used, and  
 157 the size of each one was 0.15 cm.  
 158

159 **HU-to-density relation for SECT calibrations**

160 For the calibrations, the average CT number (HU) of each material from the reconstructed images  
 161 along with the corresponding physical density (known for the calibration phantoms) were used to form  
 162 the LUTs. A fourth order polynomial was applied to relate the physical density  $\rho$  with HU in  
 163 Hounsfield units as follows:

164 
$$\rho(HU) = c_0 + c_1HU + c_2HU^2 + c_3HU^3 + c_4HU^4, \quad (1)$$

165 where  $c_i$  ( $i = 0, \dots, 4$ ) are the parameters; note,  $c_0$  can be expressed with  $c_i$  ( $i = 1, \dots, 4$ )  
 166 because  $\rho(-1000) = 0$ . Therefore, the last four can be determined from a least-squares fit to the LUT  
 167 of the SECT scans. The values of the parameters may differ depending on the X-ray energies and  
 168 calibration phantoms and should be treated accordingly.

169 **HU-to-density relation for DECT calibration**

170 The  $\Delta HU - \rho_e$  conversion method<sup>22,23</sup> was applied for the DECT calibration, however, the electron  
 171 density  $\rho_e$  was replaced with the physical density  $\rho$ . This is appropriate because  $\rho$  is proportional to

172  $\rho_e$ . The dual energy subtracted quantity  $\Delta HU$  was defined as follows:

$$173 \quad \Delta HU \equiv (1 + \alpha)HU_H - \alpha HU_L, \quad (2)$$

174 where  $HU_H$  and  $HU_L$  denote the high-energy and low-energy CT numbers in Hounsfield units,  
175 respectively. Further,  $\alpha$  is a weighting factor for the subtraction, which is regarded as material-  
176 independent. Similar to a previous study<sup>22</sup>, the relation between  $\Delta HU$  and  $\rho$  was assumed to be linear  
177 for materials with low effective atomic numbers as follows:

$$178 \quad \rho(\Delta HU) = a \frac{\Delta HU}{1000} + b, \quad (3)$$

179 where  $a$ ,  $b$ , and  $\alpha$  can be determined by a least squares fit to  $(HU_H, HU_L) - \rho$  data obtained from  
180 DECT scans of materials with a known density  $\rho$  in calibration phantoms, which is similar to the SECT  
181 calibration.

## 182 **Validation**

183 The minimum  $\chi^2$  value of the fitting curves for the physical density were evaluated for all three  
184 calibration phantoms. A total of 30 virtual images based on the ICRP110 human phantoms (shown in  
185 Table I and Figs. 3 and 4) were independently prepared via virtual projections and image reconstructions.  
186 The physical density distribution converted by the LUTs of each energy spectrum and calibration  
187 phantom were compared with the ground truth. Statistical analysis was performed to determine the  
188 differences in the RMSE among the chosen energies (for SECT), their combinations (for DECT), or the  
189 chosen calibration phantoms. In particular, the following differences were assessed: 1) between SECT  
190 and DECT, 2) between TS and BT(B), and 3) among the energies with BT(A) and BT(B). For the  
191 statistical analysis, a Student's t-test was employed for the first two cases, while Tukey's range test was  
192 employed for the last.

## 193 **Results**

### 194 **Generated sinograms and reconstructed images**

195 Fig. 7 presents the representative sinograms generated from the MBFPA of the TS phantom with four  
196 energies, and Fig. 8 presents the corresponding reconstructed images.

197

198

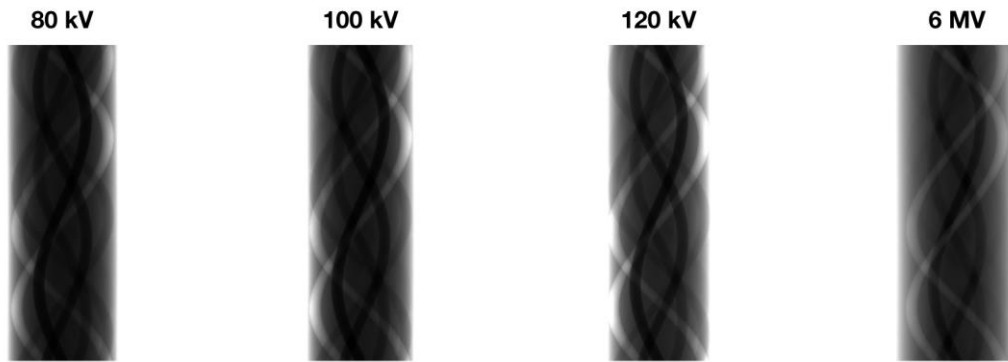


Fig. 7. Sinograms of the TS phantom with 80 kV, 100 kV, 120 kV, and 6 MV. The display value ranges are 0–0.01 for kV CT and 0.1–0.3 for MV CT.

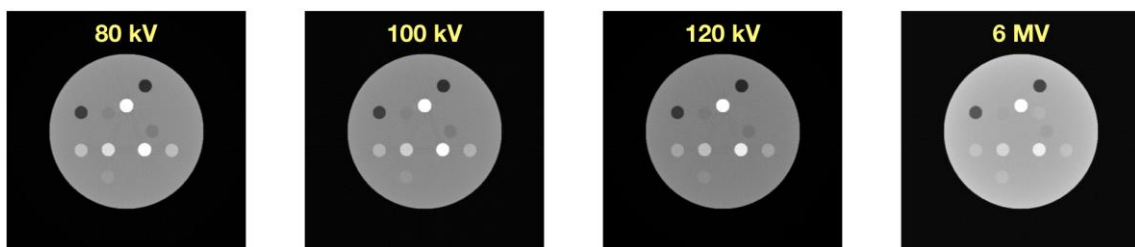


Fig. 8. Reconstructed images of the TS phantom with 80 kV, 100 kV, 120 kV, and 6 MV. The display value ranges of the attenuation coefficients (in units of  $\text{cm}^{-1}$ ) are 0–0.4 for kV CT and 0–0.1 for MV CT.

### SECT calibration results

A dataset of CT values and physical densities in the calibration phantoms can be derived from the above reconstructed images. The data points and fitted curves for all three phantoms and four energies are shown in Fig. 9. The three calibration phantoms present similar behaviours, which is reasonable because similar or same materials were used. However, the BT(A) phantoms present a relatively different behaviour compared to the TS and BT(B) phantoms in the case of 6 MV because the size of the former is smaller.

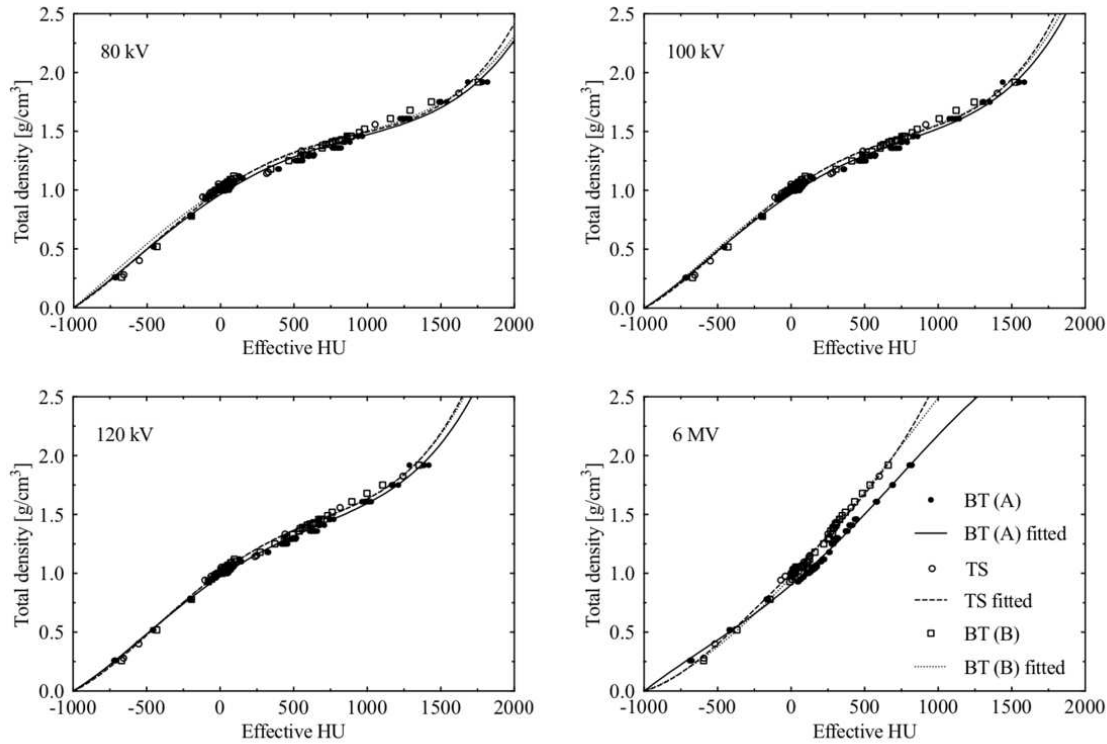
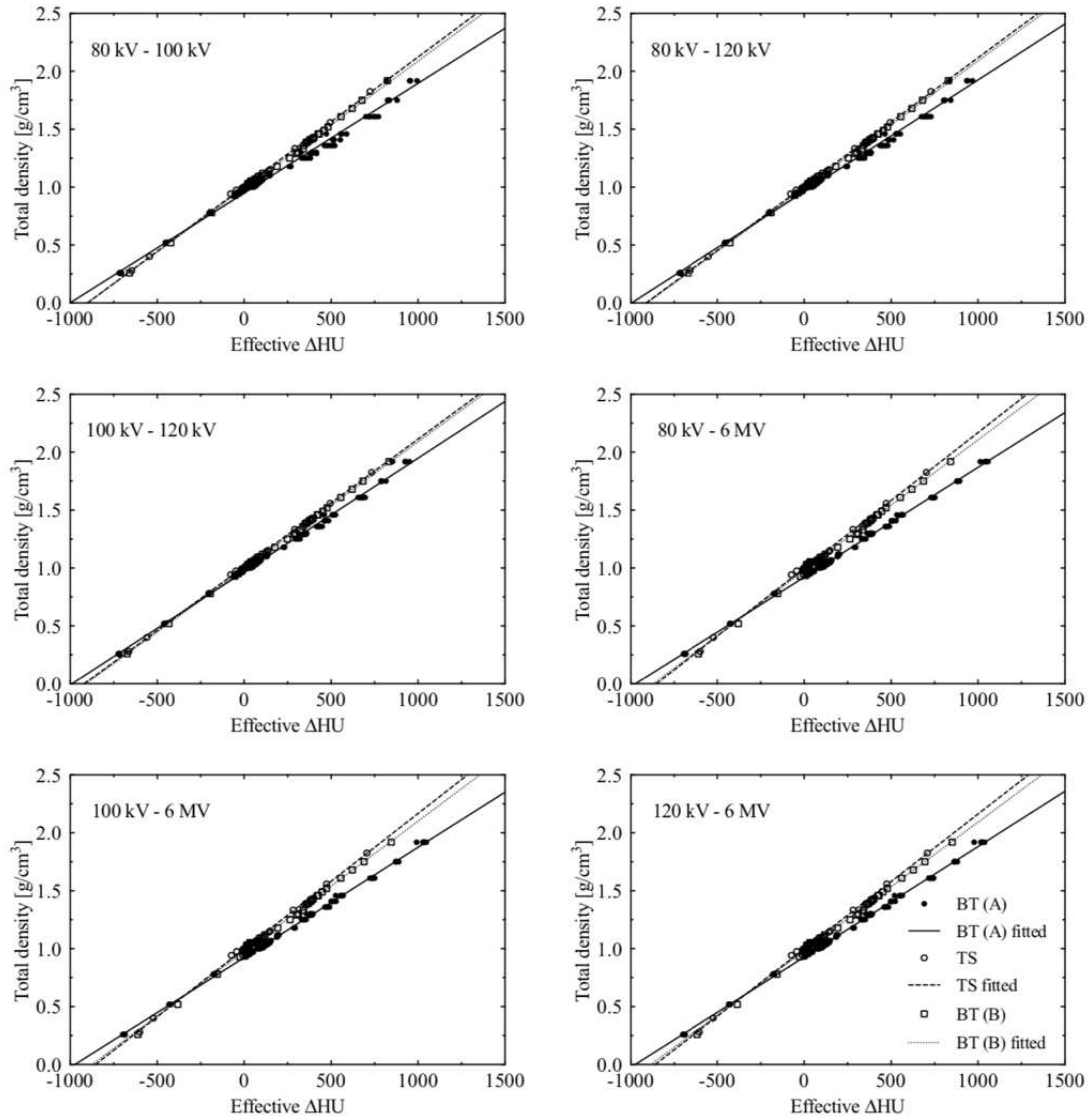


Fig. 9. HU-to-density relations of three calibration phantoms with 80 kV, 100 kV, 120 kV, and 6 MV in SECT. The CT values are referred to as “Effective HU” because this approach is based on simulations.

### DECT calibration results

The data of  $\Delta HU$  and  $\rho$ , as well as the fitted results, are shown in Fig. 10. It was found that the TS and BT(B) phantoms have similar behaviours in all six DECT calibrations, which are different from the BT(A) phantoms. However, in the case of kV SECTs, all three curves present similar behaviours, as shown in Fig. 9. This is because a fourth order polynomial was applied for the SECT fitting, while a linear relationship was assumed for the DECT calibration. Therefore, the difference in the data points is suppressed by the higher order terms in the SECT situation. However, for the DECT calibration, such differences become notable. In addition, the fact that the size/shape of BT(A) and BT(B) phantoms are different also implies that the physical density estimation in the  $\Delta HU$  approach depends on (the size/shape of) the calibration phantoms as well. In particular, this dependence appears stronger in kV-MV DECT calibrations.



233

234 Fig. 10. Effective  $\Delta$ HU to density relations of the three calibration phantoms with 80 kV, 100 kV, 120 kV,  
 235 and 6 MV in DECT.

236

237 **Validation using the ICRP110 human phantom**

238 The validation results using the ICRP110 human phantom are shown in Table II, where the average  
 239 RMSEs are listed for all the anatomies. No significant difference in the RMSEs was found between  
 240 SECT and DECT ( $p$ -values: 0.26, 0.16, and 0.68 for BT(A), TS, and BT(B), respectively). Conversely,  
 241 the predicted results from the calibrations using BT(B) phantom significantly improved compared to  
 242 that using TS phantom in density calibration ( $p$ -values:  $< 0.01$ ), although the mean RSME difference  
 243 was less than 0.0093. For the energy dependence of the physical density estimation, the RMSEs of the

244 6 MV SECT were observed to be significantly larger than those of the others for BT(B), whereas no  
 245 significant difference was observed in the use of BT(A), mainly caused by the lung area having the large  
 246 size. In addition, the RMSEs of the 6 MV SECT from BT(A) phantoms are relatively better than those  
 247 from BT(B) phantoms. More specifically, the smaller the calibration phantom, the more accurate the  
 248 validation predictions are. However, such behaviours are not apparent in the kV SECT results.

249

250 Table 2. Predicted average RMSEs of ICRP110 phantom slices from BT(A), TS, and BT(B) phantoms with SECT  
 251 and DECT.

Calibration	Anatomy	SECT predictions				DECT predictions					
		80 kV	100 kV	120 kV	6 MV	80 kV-100 kV	80 kV-120 kV	100 kV-120 kV	80 kV-6 MV	100 kV-6 MV	120 kV-6 MV
BT(A)	Head	0.1230	0.1236	0.1197	0.1270	0.1264	0.1180	0.1128	0.1155	0.1160	0.1156
	Lung	0.1507	0.1429	0.1356	0.0978	0.1548	0.1394	0.1516	0.0950	0.0963	0.0978
	Pelvis	0.0793	0.0756	0.0739	0.0750	0.0793	0.0781	0.0785	0.0759	0.0754	0.0750
TS	Head	0.1362	0.1424	0.1395	0.2289	0.1758	0.1542	0.1395	0.1981	0.1967	0.1934
	Lung	0.1589	0.1522	0.1445	0.1237	0.1873	0.1595	0.1728	0.1144	0.1141	0.1135
	Pelvis	0.0759	0.0762	0.0770	0.1267	0.0951	0.0917	0.0903	0.1121	0.1108	0.1089
BT(B)	Head	0.1294	0.1375	0.1368	0.2217	0.1644	0.1454	0.1327	0.1771	0.1749	0.1702
	Lung	0.1484	0.1456	0.1418	0.1172	0.1809	0.1558	0.1687	0.1046	0.1048	0.1050
	Pelvis	0.0727	0.0745	0.0757	0.1144	0.0876	0.0850	0.0842	0.0934	0.0918	0.0896

252

## 253 **Discussions**

254 This study presented the evaluation of both SECT and DECT calibrations based on the MBFPA and  
 255 demonstrated that the accuracy of SECT calibration is comparable with that of DECT. In addition, the  
 256 use of the biological tissue phantom in the calibration was found to improve the physical density  
 257 prediction compared with that of the Gammex phantom composed of tissue substitutes.

258 Similar results have already been implicitly obtained by Goma et al. who performed SECT calibration  
 259 using the stoichiometric method, which consists of characterising the CT scanner directly through CT  
 260 scans of tissue substitutes, and subsequently predicting the CT numbers of biological tissues using this  
 261 characterisation<sup>9</sup>. The main difference between the stoichiometric calibration and the present MBFPA  
 262 approach is that the former requires real CT images acquired from CT scanners, whereas the latter does

263 not. In this study, the CT scanners were modelled, characterised by X-ray energy spectra directly, by  
264 which various simulations, with not only the kV-range X-rays but also MV-range X-rays, could be  
265 performed. Furthermore, the density results cannot be validated for real patients in the stoichiometric  
266 calibration framework. However, using the proposed MBFPA-based calibration approach, the validation  
267 is now possible by preparing, for example, the reconstructed CT datasets using the ICRP110 human  
268 phantom, which could be considered as real patients to a certain extent. This study not only supported  
269 the results of Goma et al.<sup>9</sup> but also newly presented that the tissue substitutes differ from the biological  
270 tissues in physical density calibration.

271 The results of this study indicated that kV-MV DECT is not as outperformed as it was expected to be.  
272 This is due to the large beam hardening effect in MV CT, compared to that in kV CT. This can be inferred  
273 from the fact that different sizes of the calibration phantoms provided different calibration curves with  
274 MV X-rays. For a more apparent indication, a simulation using monochromatic energy X-rays with 3  
275 MeV was also performed, which does not suffer from beam hardening. In this case, no phantom size  
276 dependence in the calibration curves was observed. The magnitude of beam hardening in MV CT could  
277 also be observed in the homogeneous water phantom (of the same size as the TS phantom) by extracting  
278 the reconstructed CT values in the centre and peripheral regions. Their relative difference was ~17% for  
279 MV CT due to the cupping artefacts; however, this value is only ~10% for kV CT. Such ambiguity in  
280 the MV CT with a practical spectrum significantly affected the accuracy of the calibration. Hence, DECT  
281 with MV X-rays does not improve the accuracy of the physical density estimation as well as the SECT  
282 of MV X-rays. Furthermore, the use of MV X-rays passing through a titanium filter could, to a certain  
283 extent, reduce the beam-hardening effect.

284 Note that Yang et al. assessed the superiority of kV-MV DECT in determining proton stopping power  
285 by generating 1 MV beams from MC calculations<sup>24</sup>. According to the authors, *when CT number*  
286 *uncertainties and artefacts such as imaging noise and beam hardening effects were considered, the kV-*  
287 *MV DECT improved the perfectly of SPR estimation substantially over kV-kV or MV-MV DECT methods.*  
288 The SPR estimation is directly influenced by the electron density (or physical density), and therefore,  
289 Yang et al.'s study implied a substantial decrease in the physical density uncertainties in kV-MV DECT.  
290 However, this study apparently supports the contrary. This might indicate that the beam hardening

291 effects were underestimated in MV CT in Yang et al.'s study because the authors assumed the "average  
292 spectra" accurately modelled the CT scanner. Thus, the beam hardening effect should be carefully  
293 treated in MV CT.

294 The proposed method can be considered an improvement over previous stoichiometric approaches in  
295 which the parameters, depending on the X-ray spectrum, which characterise the CT scanner are  
296 determined by fitting to the effective linear attenuation coefficients of a given material, whereas the  
297 proposed method explicitly deals with the X-ray spectrum. Although the explicit handling of the X-ray  
298 spectrum is advantageous in CT calibration, the requirement of the X-ray spectrum imposes limitations  
299 for practical applications. That is, the exact energy spectrum of medical CT scanners is unknown, and  
300 its direct measurement is difficult because of the high photon flux. Nevertheless, novel methods to  
301 estimate X-ray spectra in practical CT scanners have been proposed in recent years<sup>25-27</sup>. Therefore, it is  
302 reasonable to assume that X-ray spectra are currently available.

303

#### 304 **Conclusions**

305 The proposed method using the MBFPA is useful in the theoretical analysis of physical density  
306 calibrations. The accuracy of SECT calibration is comparable with that of DECT calibration and is  
307 improved with the use of biological tissues. The size and shape of the calibration phantom could affect  
308 the accuracy, especially for MV CT, mainly because of the beam hardening effects. The present method  
309 based on the MBFPA can also be applied to various other studies, such as effective atomic number  
310 estimations and material decompositions.

311

312 **Declarations**

313 **Ethics approval and consent to participate**

314 Not applicable.

315 **Consent for publication**

316 Not applicable.

317 **Availability of data and materials**

318 The datasets used and/or analysed during the current study are available from the corresponding author  
319 upon reasonable request.

320 **Competing interests**

321 The authors declare that they have no competing interests.

322 **Funding**

323 This work was partially supported by JSPS KAKENHI (Grant No. 19K08201) and by the National  
324 Natural Science Foundation of China (Grant No. 11735003).

325 **Authors' contributions**

326 KL and DF conceived the idea. The method was discussed for KL, DF, and AH. Based on the discussion,  
327 KL and AH developed the software, and KL and DF analysed the generated data. KL, AH, HL, and LG  
328 presented the obtained results. KL and AH drafted the manuscript. All authors read, modified, and  
329 approved the manuscript.

330 **Acknowledgements**

331 The authors thank Elekta for providing the structural information of the scanner heads for the MC  
332 simulation of XVI systems.

333

334 **Appendix: Material-based forward projection algorithm (MBFPA)**

335 The material-based forward projection algorithm applied in the X-ray virtual projections is briefly  
 336 introduced here. According to Lambert-Beer's law, the photon number  $n_i$  in the  $i$ -th detector after  
 337 penetrating the object with attenuation coefficient  $\mu_j$  in voxel  $j$  is as follows:

$$338 \quad n_i(E) = n_0(E)e^{\sum_j -a_{ij}\mu_j(E)}, \quad (A1)$$

339 where  $E$  is the photon energy,  $n_0$  is the photon number in the X-ray source, and  $a_{ij}$  is the photon  
 340 pass length in voxel  $j$ , representing an element of the “system matrix”. If the spectrum of the X-ray is  
 341 considered (as bins), the total photon number in the  $i$ -th detector becomes the following:

$$342 \quad n_i^{total} = \sum_E \alpha(E)n_i(E) = \sum_E \alpha(E)n_0(E) e^{\sum_j -a_{ij}\mu_j(E)}, \quad (A2)$$

343 where  $\alpha(E)$  is the fraction of the corresponding photon energy bin.  $\mu_j(E)$  is dependent on the atomic  
 344 number  $Z$  and the density  $\rho$  of the materials in a voxel  $j$ , which is expressed as a sum of the  
 345 attenuation coefficients for each element  $m$  as follows:

$$346 \quad \mu_j(E, Z, \rho) = \sum_m w_m \mu_{m,j}(E, Z, \rho), \quad (A3)$$

347 where  $w_m$  denotes the weight (fraction) of the  $m$ th element. For the energy range considered in this  
 348 study, the attenuation coefficient  $\mu_{m,j}(E, Z, \rho)$  can be written as the sum of the processes of the  
 349 photoelectric effect, Compton scattering, and pair production as follows:

$$350 \quad \mu_{m,j}(E, Z, \rho) = \rho Z \frac{N_A}{A} [\sigma_{pe}(E, Z) + \sigma_{comp}(E) + \sigma_{pp}(E, Z)], \quad (A4)$$

351 where  $N_A$  and  $A$  denote the Avogadro constant and atomic weight, respectively.  $\sigma$  is the cross section  
 352 of the photon – matter interactions. The cross section of the photoelectric effect can be approximated  
 353 by<sup>28</sup> as follows:

$$354 \quad \sigma_{pe}(E, Z) = 3.45 \times 10^{-6} r_e^2 (1 + 0.008Z) \frac{Z^3}{E^3} \left(1 - \frac{E_k}{4E} - \frac{E_k^2}{1.21E}\right), \quad (A5)$$

355 where  $r_e = 2.81794$  fm is the classical electron radius and  $E_k$  is the  $K$ -shell binding energy. The  
 356 latter is ignored in this study. The Compton scattering cross section is theoretically expressed by the  
 357 Klein–Nishina formula as follows:

358 
$$\sigma_{comp}(E) = 2\pi r_e^2 \left\{ \frac{1+E}{E^2} \left[ \frac{2(1+E)}{1+2E} - \frac{\ln(1+2E)}{E} \right] + \frac{\ln(1+2E)}{2E} - \frac{1+3E}{(1+2E)^2} \right\}. \quad (A6)$$

359 The cross section of the pair production is approximated as<sup>28</sup> follows:

360 
$$\sigma_{pp}(E, Z) = 0.2545 r_e^2 (E - 2.332) \frac{Z}{137}. \quad (A7)$$

361 As a result, the virtual projections were simulated by a ray-tracing method to generate sinograms. The  
362 sinograms were simulated by considering the energy spectrum with a bin width of 1 keV in this study.

363

364 **References**

- 365 1. Mull RT. Mass estimates by computed tomography: physical density from CT numbers. *Am J*  
366 *Roentgenol* 1984;143(5):1101-1104.
- 367 2. Langen KM, Meeks SL, Poole DO, Wagner TH, Willoughby TR, Kupelian PA, Ruchala KJ,  
368 Haimerl J, Olivera GH. The use of megavoltage CT (MVCT) images for dose recomputations.  
369 *Phys Med Biol* 2005;50(18):4259.
- 370 3. Yang Y, Schreibmann E, Li T, Wang C, Xing L. Evaluation of on-board kV cone beam CT  
371 (CBCT)-based dose calculation. *Phys Med Biol* 2007;52(3):685.
- 372 4. Verhaegen F, Devic S. Sensitivity study for CT image use in Monte Carlo treatment planning.  
373 *Physics in Medicine & Biology*, 50:937, 2005.
- 374 5. Fang R, Mazur T, Mutic S, Khan R, The impact of mass density variations on an electron Monte  
375 Carlo algorithm for radiotherapy dose calculations. *Phys Imag Radiat Oncol* 2018;8:1.
- 376 6. Cozzi L, Fogliata A, Buffa F, Bieri S. Dosimetric impact of computed tomography calibration on  
377 a commercial treatment planning system for external radiation therapy. *Radiother Oncol*  
378 1998;48(3):335-338.
- 379 7. Schaffner B, Pedroni E. The precision of proton range calculations in proton radiotherapy  
380 treatment planning: experimental verification of the relation between CT-HU and proton stopping  
381 power. *Phys Med Biol* 1998;43(6):1579.
- 382 8. Schneider U, Pedroni E, Lomax A. The calibration of CT Hounsfield units for radiotherapy  
383 treatment planning. *Phys Med Biol* 1996;41(1):111.
- 384 9. Gomá C, Almeida IP, Verhaegen F. Revisiting the single-energy CT calibration for proton therapy  
385 treatment planning: a critical look at the stoichiometric method. *Phys Med Biol*  
386 2018;63(23):235011.
- 387 10. Michalak G, Taasti V, Krauss B, Deisher A, Halawish A, McCollough C. A comparison of  
388 relative proton stopping power measurements across patient size using dual- and single-energy  
389 CT. *Acta Oncol* 2017;56:1465-71.

- 390 11. Yang M, Virshup G, Clayton J, Zhu XR, Mohan R, Dong L. Theoretical variance analysis of  
391 single-and dual-energy computed tomography methods for calculating proton stopping power  
392 ratios of biological tissues. *Phys Med Biol* 2010;55(5):1343.
- 393 12. Hunemohr N, Paganetti H, Greilich S, Jakel O, Seco J. Tissue decomposition from dual energy ct  
394 data for mc based dose calculation in particle therapy. *Med Phys* 2014;41(6Part1):061714.
- 395 13. II ICRU. Tissue substitutes in radiation dosimetry and measurement. *International Commission on*  
396 *Radiation Units and Measurements*, 1989.
- 397 14. White DR, Woodard HQ, Hammond SM. Average soft-tissue and bone models for use in radiation  
398 dosimetry. *Brit J Radiol* 1987;60(717):907-913.
- 399 15. Woodard HQ, White DR. The composition of body tissues. *Brit J Radiol* 1986;59(708):1209-  
400 1218.
- 401 16. Elbakri, IA, Fessler JA. Statistical image reconstruction for polyenergetic x-ray computed  
402 tomography. *IEEE Trans Med Imaging* 2002;21(2):89-99.
- 403 17. Shen L, Xing Y. Multienergy CT acquisition and reconstruction with a stepped tube potential  
404 scan. *Med Phys* 2015;42(1):282-296.
- 405 18. Ruchala KJ, Olivera GH, Schloesser EA, Mackie TR: Megavoltage CT on a tomotherapy system.  
406 *Phys Med Biol* 1999;44:2597-2621.
- 407 19. Wertz H, Stsepankou D, Blessing M, Rossi M, Knox C, Brown K, Gros U, Boda-Heggemann J,  
408 Walter C, Hesser C, Lohr F, Wenz F: Fast kilovoltage/megavoltage (kVMV) breathhold cone-  
409 beam CT for image-guided radiotherapy of lung cancer, *Phys Med Biol* 2010;55:4203-4217.
- 410 20. Pouliot J, Bani-Hashemi A, Chen J, et al. Low-dose megavoltage cone-beam CT for radiation  
411 therapy. *Int J Radiat Oncol Biol Phys* 2005;61:552-560.
- 412 21. Sakata D, Haga A, Kida S, Imae T, Takenaka S, Nakagawa K. Effective atomic number  
413 estimation using kV-MV dual-energy source in linac. *Phys Medica*, 2017;39:9-15.
- 414 22. Saito M. Potential of dual-energy subtraction for converting CT numbers to electron density based  
415 on a single linear relationship. *Med Phys* 2012;39.
- 416 23. Tsukihara M, Noto Y, Sasamoto R, Hayakawa T, Saito M. Initial implementation of the  
417 conversion from the energy-subtracted CT number to electron density in tissue inhomogeneity

- 418 corrections: An anthropomorphic phantom study of radiotherapy treatment planning. *Med Phys*  
419 2015;42.
- 420 24. Yang M, Virshup G, Clayton J, Zhu XR, Mohan R, Dong L. Does kV–MV dual-energy computed  
421 tomography have an advantage in determining proton stopping power ratios in patients? *Phys Med*  
422 *Biol* 2011;56(14):4499.
- 423 25. Sidky EY, Yu L, Pan X, Zou Y, Vannier M. A robust method of x-ray source spectrum estimation  
424 from transmission measurements: Demonstrated on computer simulated, scatter-free transmission  
425 data. *J Appl Phys* 2005;97(12):124701.
- 426 26. Duan X, Wang J, Yu L, Leng S, McCollough CH. CT scanner x-ray spectrum estimation from  
427 transmission measurements. *Med Phys* 2011;38(2):993-997.
- 428 27. Ha W, Sidky EY, Barber RF, Schmidt TG, Pan X. Estimating the spectrum in computed  
429 tomography via Kullback–Leibler divergence constrained optimization. *Med Phys* 2019;46(1):81-  
430 92.
- 431 28. Yao W, Leszczynski KW. An analytical approach to estimating the first order x-ray scatter in  
432 heterogeneous medium. *Med Phys* 200936(7):3145-3156.

433

434

---

435

# Figures

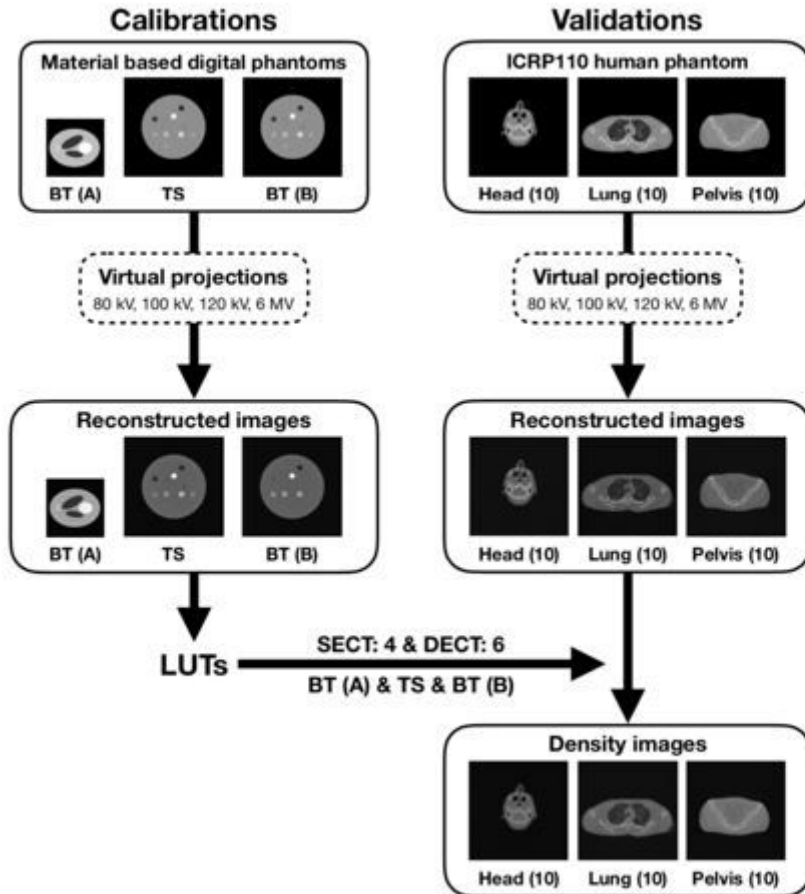
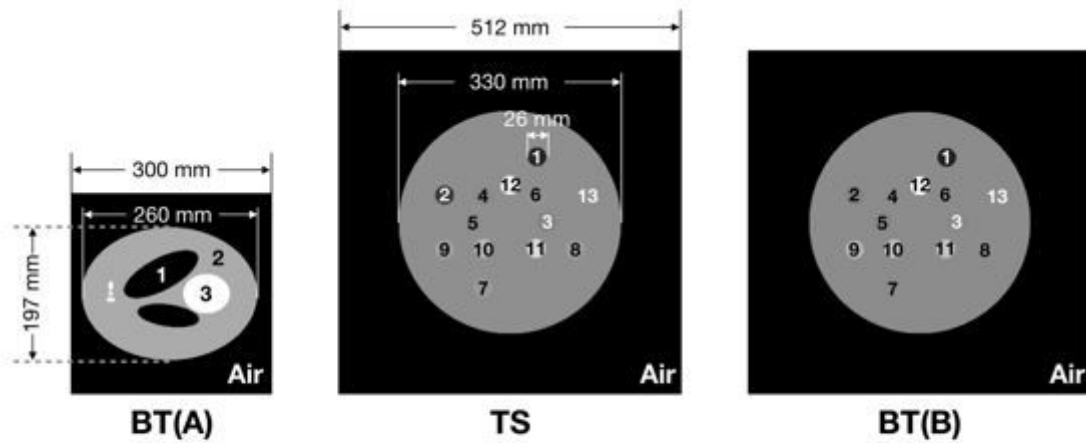


Figure 1

Workflow of the current study for total density evaluation. BT(A), TS, and BT(B) phantoms were used for the calibration, and the ICRU human phantoms were used for the validation (for more details, see the main text).



- **BT(A)** 1-3: biological tissues
- **TS** 1: LN-300, 2: LN-450, 3: AP6, 4: BR12, 5: Water, 6: SR2, 7: LV1, 8: IB3, 9: B200, 10: CB2-30%CaCO<sub>3</sub>, 11: CB2-50%CaCO<sub>3</sub>, 12: SB3, 13: Solid water
- **BT(B)** 5: Water, **Others**: biological tissues

**Figure 2**

Shape, size, and composition of the BT(A), TS, and BT(B) phantoms in the calibration.

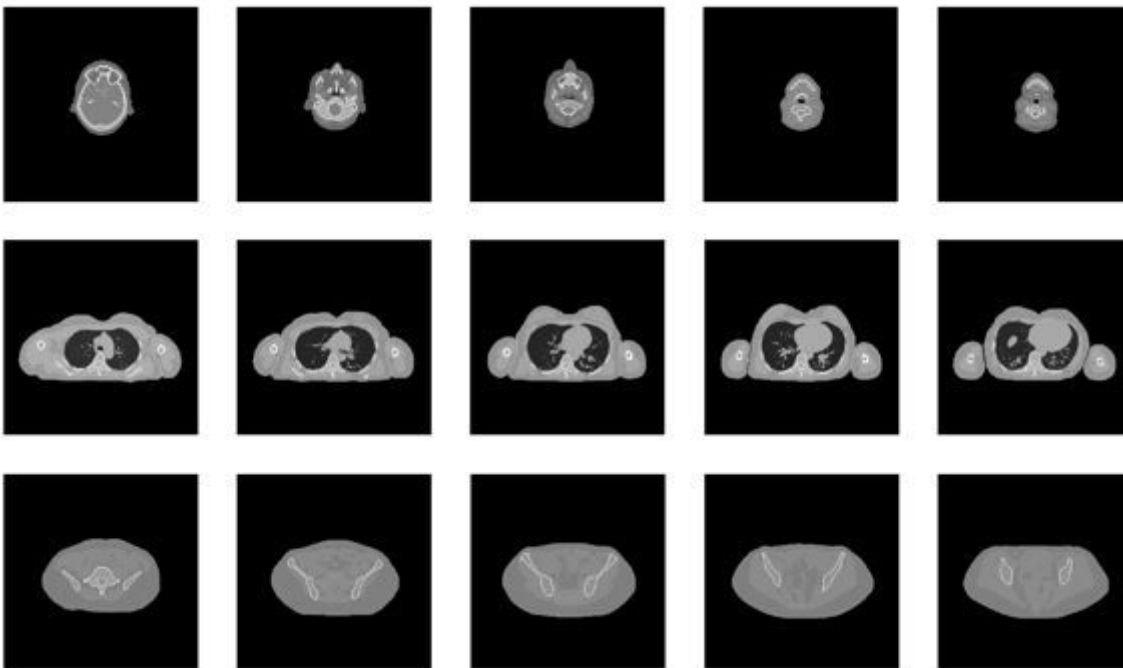


**Figure 3**

Ground truth of the selected ICRP110 human phantoms for female. The images in the first, second, and third row indicate head, lung, and pelvis, respectively.

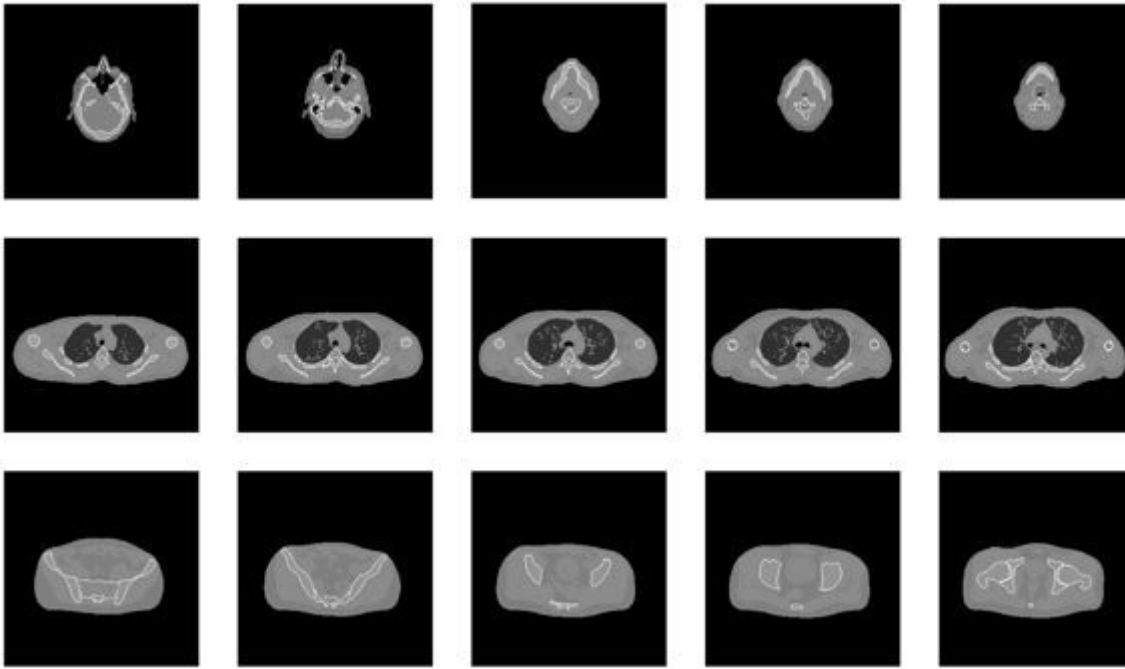


**Figure 4**

Ground truth of the selected ICRP110 human phantoms for male. The images in the first, second, and third row indicate head, lung, and pelvis, respectively.

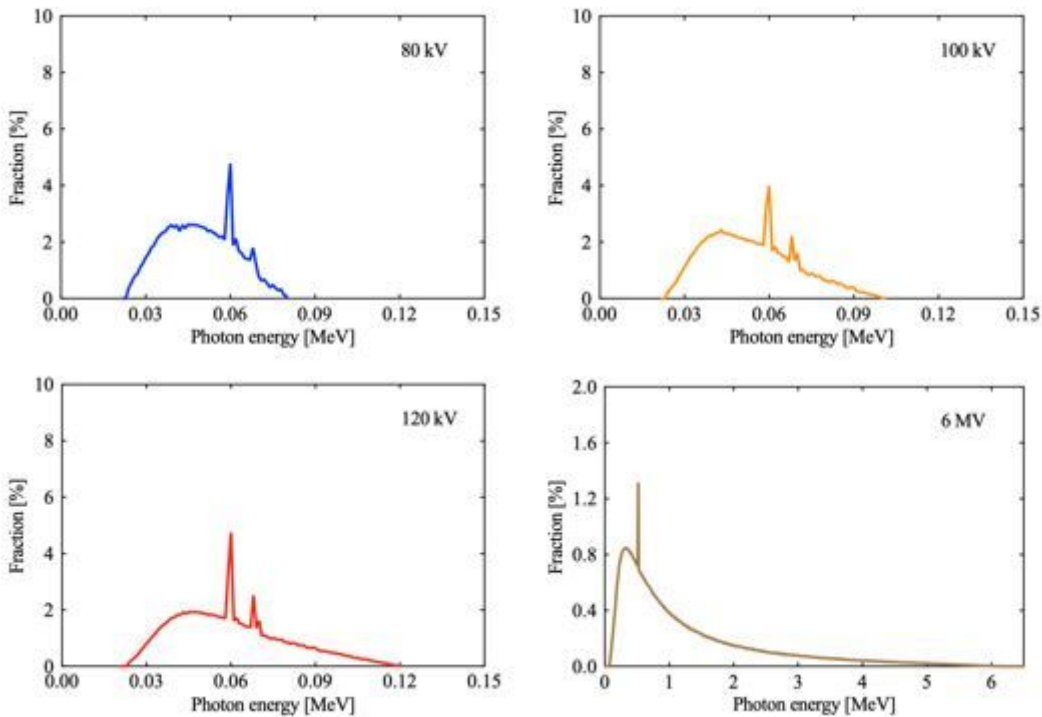


**Figure 5**

Simulated X-ray spectra of 80 kV, 100 kV, 120 kV, and 6 MV. The mean energies were 48.70 keV, 53.24 keV, 59.28 keV, and 1.30 MeV, respectively.

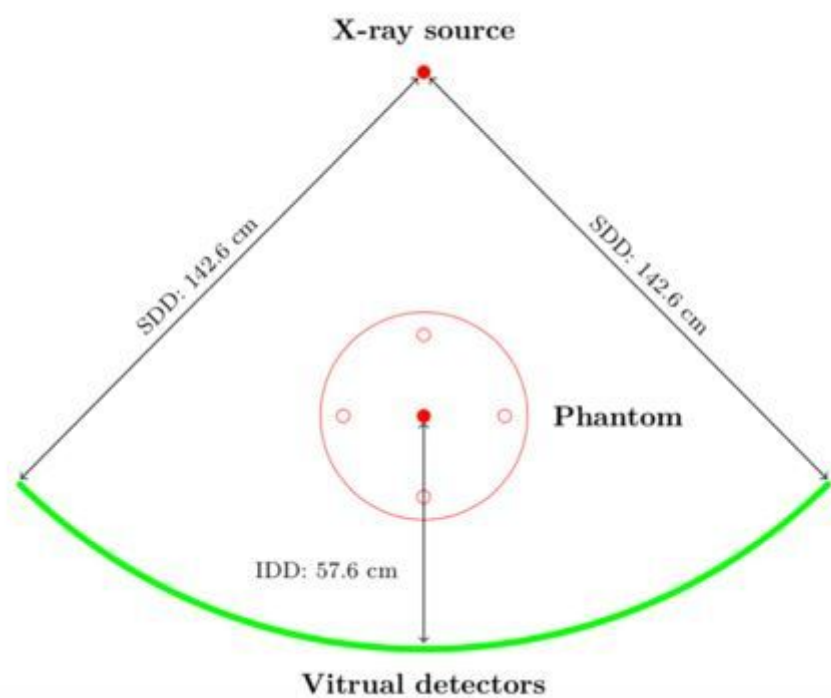


**Figure 6**

Schematic of geometry applied in sinogram production. IDD and SDD indicate the isocenter-to-detector distance and the source-to-detector distance, respectively. A total of 609 detectors were used, and the size of each one was 0.15 cm.

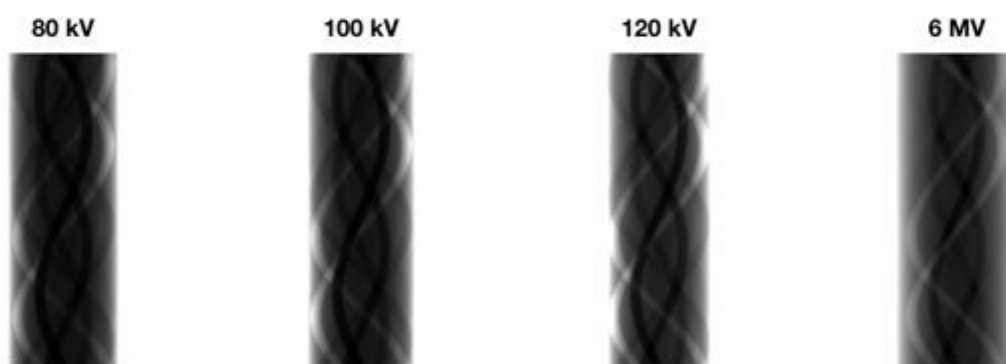


**Figure 7**

Sinograms of the TS phantom with 80 kV, 100 kV, 120 kV, and 6 MV. The display value ranges are 0–0.01 for kV CT and 0.1–0.3 for MV CT.

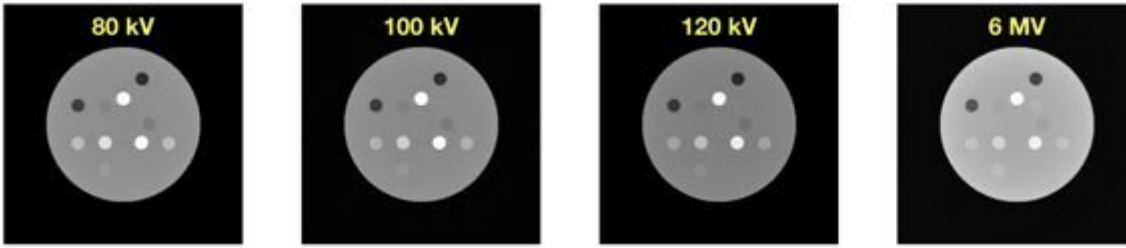


Figure 8

Reconstructed images of the TS phantom with 80 kV, 100 kV, 120 kV, and 6 MV. The display value ranges of the attenuation coefficients (in units of  $\text{cm}^{-1}$ ) are 0–0.4 for kV CT and 0–0.1 for MV CT.

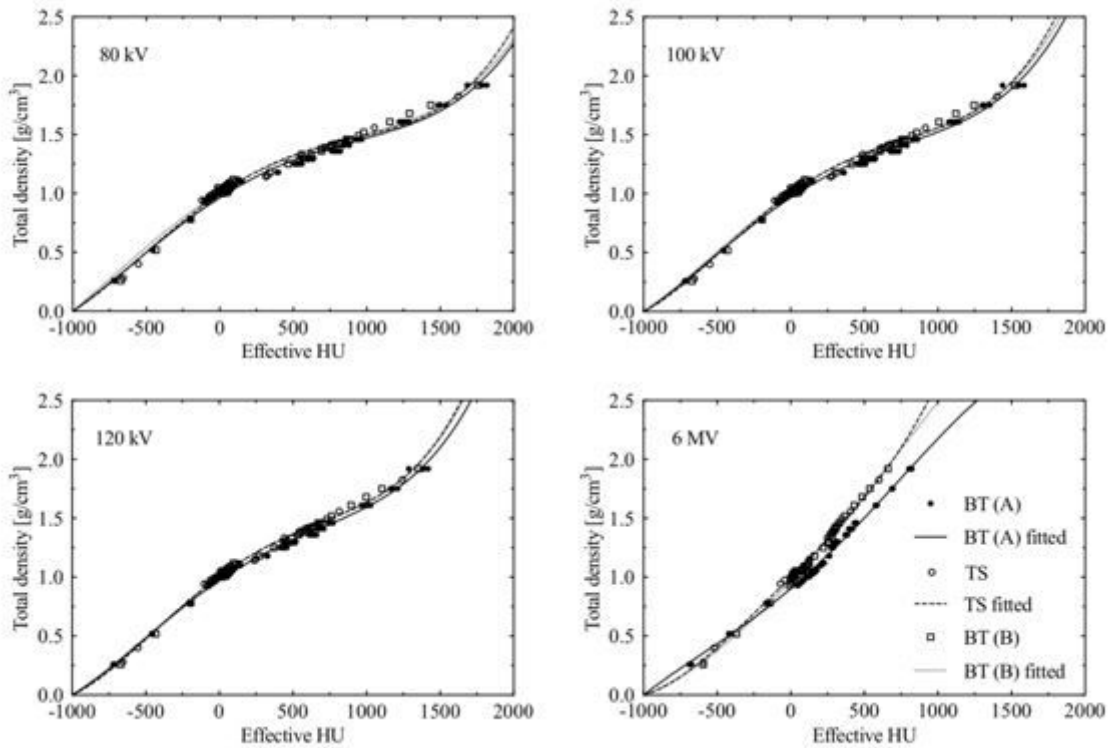
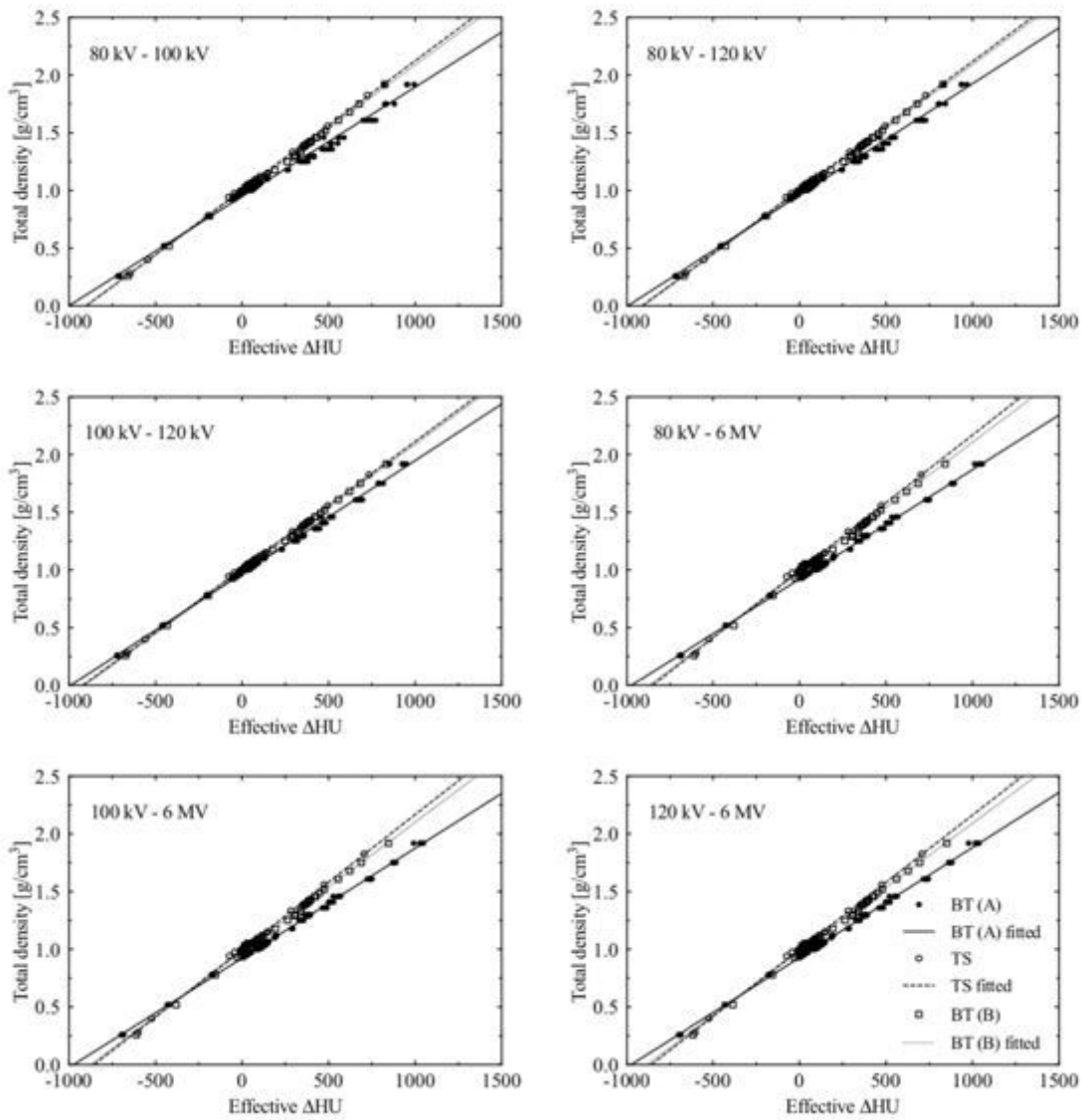


Figure 9

HU-to-density relations of three calibration phantoms with 80 kV, 100 kV, 120 kV, and 6 MV in SECT. The CT values are referred to as “Effective HU” because this approach is based on simulations.



**Figure 10**

Effective  $\Delta$ HU to density relations of the three calibration phantoms with 80 kV, 100 kV, 120 kV, and 6 MV in DECT.